17th Australasian Fluid Mechanics Conference
Auckland, New Zealand
5-9 December 2010

Analysis of Ornithopter-Wing Aerodynamics

A. Valiyff, J. R. Harvey, M. B. Jones, S. M. Henbest, and J. L. Palmer

Air Vehicles Division, Defence Science and Technology Organisation, Fishermans Bend, VIC, 3207 Australia

Abstract

The aim of the work presented in this paper is to characterise the flapping-flight aerodynamics of ornithopter wings through experimentation and analysis. Time-resolved and mean measurements have been made of the thrust produced by two commercially available ornithopters in a low-speed wind tunnel at varying air speeds and flapping frequencies. In order to gain a better understanding of flapping flight and for comparison with the experimental results, an aerodynamic model relying on blade-element theory has been utilised.

Introduction

Accurate aerodynamic modelling of the flapping flight of insects, birds, and bats and their mechanical counterparts (insect- and bird-like devices, known as entomopters and ornithopters, respectively) is difficult, due to the relatively low Reynolds numbers at which most operate and the typically low aspect ratios of their wings, which promote strong tip vortices and rolling instabilities. Furthermore, accounting for wing structural flexibility is a complex task and therefore is generally neglected.

Several attempts have been made previously to characterise the aerodynamics of flapping-wing micro air vehicles (MAVs) by use of experimental and analytical methods. Hu *et al.* [5] and Motamed and Yan [8] performed force measurements with bench-top flapping mechanisms. Although not appropriate for implementation in a functional MAV (given the significant size and weight of the driving mechanisms), their approaches permitted accurate force measurements to be conducted with complex wing kinematics. Other researchers have made force measurements directly on operational MAVs. For example, Mueller *et al.* [9] recently developed a test stand for measuring the time-resolved thrust and lift generated by a 15-g flapping-wing MAV.

The focus of this study was to characterise the aerodynamics of two commercially available ornithopters using experimental and analytical methods. Tests were performed in a low-speed wind tunnel, where the thrust generated by each ornithopter was measured using a load sensor at various air speeds and flapping frequencies. The time-resolved and mean thrust measurements were compared with analytical predictions obtained from a blade-element model.

Blade-Element Aerodynamic Model

Aerodynamic models of flapping-wing flight fall into two distinct categories, those that account for unsteady effects through extensive modelling of the wake and those relying on an assumption that the flow is quasi-steady. In quasi-steady models, the details of the wake are rendered less important by the assumption that the flapping frequency is low enough that shed-wake effects are insignificant.

In this paper, the blade-element approach by DeLaurier [2] has been selected as the basis of a quasi-steady aerodynamic model. The following is a brief outline; for a comprehensive review, refer to [2]. The wing is flapped by a periodic variation of its root-dihedral angle, and the prescribed deflections of the structure generate a spanwise twist distribution. The model accounts for partial leading-edge suction and post-stall behaviour, as well as vortex-wake effects [2, 3].

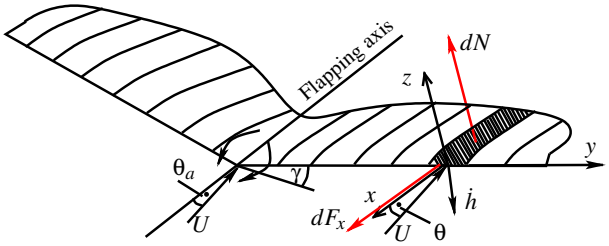

Figure 1: Root-flapping wing (adapted from [2]).

The wing leading edge is taken to be a rigid axis about which wing twist occurs, and the magnitude of the wing twist is a prescribed function of spanwise coordinate (y) and time (t). The wing is divided into a finite number of segments, each of which is analysed independently. As indicated in figure 1, the x and y axes lie along the chord and span of a given wing section, respectively. The motion of each section consists of a plunging velocity at the leading edge ($\dot{h}$) and a local pitch angle (θ). The plunging displacement (h) is described by

$$h(y,t) = \Gamma y \cos(\omega t), \tag{1}$$

where Γ is the maximum flapping angle and ω is the flapping rate ($\omega = 2\pi f$, where f is in Hz and ω is in rad/s). The pitch angle (θ) is the sum of: the angle of the flapping axis with respect to the freestream (θ_a); the mean pitch of the chord with respect to the flapping axis (θ_w); and the dynamically varying pitch angle ($\delta\theta$), which is due to the prescribed wing twist. Thus,

$$\theta(y,t) = \theta_a + \theta_w(y) + \delta\theta(y,t), \tag{2}$$

where

$$\delta\theta(y,t) = -\beta_0 y \sin(\omega t) \tag{3}$$

and β_0 is a constant representing the twist angle per unit distance along the span.

Figure 2 shows the orientations and positions of the forces acting on a wing section, where the elemental forces have been resolved in the chordwise (x) and normal (z) directions. Each wing segment operates in one of two distinct flight regimes, attached or separated flow, determined by the relative angle of attack at the leading edge.

The normal force (dN) acting on each section is

$$dN = \begin{cases} dN_c - dN_a & \text{for attached flow} \\ (dN_c)_{sep} - (dN_a)_{sep} & \text{for separated flow,} \end{cases} \tag{4}$$

where dN_c is the normal force due to circulation, dN_a is the normal force due to apparent mass, and the subscript "sep" denotes these forces for the case of separated flow. For attached flows, the circulatory force is given by

$$dN_c = \frac{\rho U V}{2} C_n(y) c\, dy, \tag{5}$$

where V is the velocity of the flow relative to the wing at the one-quarter-chord location, U is the freestream flow velocity, ρ is the density of the fluid, $C_n(y)$ is the normal-force coefficient, and c is the local chord length. From potential-flow theory,

$$C_n = 2\pi(\alpha'(t) + \alpha_0 + \theta_a + \theta_w), \tag{6}$$

where α_0 is the angle of the section's zero-lift line and $\alpha'(t)$ is the time varying "induced" angle of attack due to the wing motion and includes a component due to downwash [2]. As the airfoil oscillates, the fluid surrounding it exerts an inertial reaction due to the accelerating fluid mass. This is known as the "force due to apparent mass" and is evaluated at the half chord. It is given by

$$dN_a = \frac{\rho\pi c^2}{4}\dot{V}_n dy, \tag{7}$$

where $\dot{V}_n$ is the rate of change of (V_n), the mid-chord normal-velocity component of $(\hat{V})$. For the case of separated flow, the element is taken to act as a bluff body; hence,

$$(dN_c)_{sep} = (C_d)_{cf}\frac{\rho\hat{V}V_n}{2}cdy, \tag{8}$$

where $(C_d)_{cf}$ is the drag coefficient for a body in crossflow, which acts as a stall normal-force coefficient here, and $\hat{V}$ is the total relative velocity at the mid-chord. The apparent-mass force for the separated case is taken to be half the value calculated for the attached case.

The net force acting in the x-direction on a blade element is given by

$$dF_x = \begin{cases} dT_s - dD_c - dD_f & \text{for attached flow} \\ 0 & \text{for separated flow,} \end{cases} \tag{9}$$

where dT_s is the force due to leading-edge suction, dD_c is the force due to aerofoil camber, and dD_f is the force due to skin friction. The leading-edge suction force, due to the sharp diversion of the flow around the leading edge [2, 3] is given by

$$dT_s = \eta_s 2\pi(\alpha' + \theta_a - \frac{c\dot{\theta}}{4U})\frac{\rho UV}{2}cdy. \tag{10}$$

An efficiency term (η_s) accounts for the effect that viscosity has on dT_s: a decrease in its magnitude, compared with that predicted by potential-flow theory. The drag force due to camber, according to potential-flow theory, is given by

$$dD_c = -2\pi\alpha_0(\alpha' + \theta_a + \theta_w)\frac{\rho UV}{2}cdy. \tag{11}$$

The drag due to skin friction is given by

$$dD_f = \frac{\rho V_x^2}{2}(C_d)_f cdy, \tag{12}$$

where V_x is the relative flow speed tangential to the section. $(C_d)_f$ is the drag coefficient due to laminar skin friction, given by $(C_d)_f = 1.328\sqrt{Re}$, where Re is the Reynolds number based on local chord length [4].

The equations for the instantaneous lift (dL) and net thrust (dT) on the section are

$$dL = [dN\cos(\theta) + dF_x\sin(\theta)]\cos(\gamma) \tag{13}$$

and

$$dT = dF_x\cos(\theta) - dN\sin(\theta), \tag{14}$$

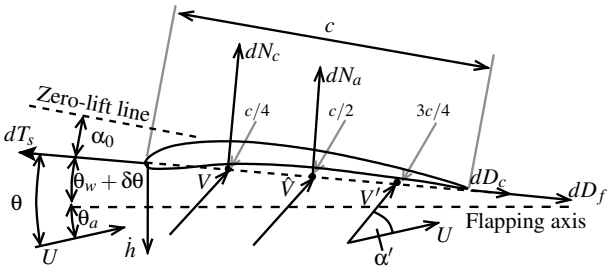

Figure 2: Wing section with resolved forces, angles, and velocities used in the analysis identified (adapted from [2]).

respectively, where γ is the dihedral angle of the blade element, as shown in figure 1. The instantaneous lift and thrust for the wing may be obtained by integrating equations (13) and (14) over the span. The net mean lift $(\overline{L})$ and thrust $(\overline{T})$ over a wingbeat cycle are obtained by averaging the instantaneous aerodynamic forces of each section.

Experimental Method

Apparatus

The experiments were performed in a closed-circuit, single-return wind tunnel, with a test section 2.7-m wide and 2.1-m high. The models were two commercially purchased ornithopters [7] with the properties listed in table 1. Measurements of the wing planform indicated that the ornithopters to be geometrically similar with a scale factor of 1.85. In each case, flapping motion is generated by a rotating crank mechanism driven by a brushless electric motor, creating a maximum flapping rate of ~ 9 Hz. The test rig, shown in figure 3, was designed to constrain the motion of the model in all directions, excluding that parallel to the flow (generated by thrust and drag). Linear bearings provided these constraints, while minimally inhibiting the axial movement of the ornithopter through friction. For the results presented here, the flapping axis was parallel to the flow ($\theta_a = 0$).

The time-dependent thrust produced by the model was measured by use of an ATI Nano17 load sensor with a resolution of 0.005 N [1]; and a National Instruments data-acquisition card was used to interpret the output of the load sensor and to record the force at a sampling frequency of 2 kHz. Although the balance is capable of measuring forces and moments in three directions, the physical constraints of the system required force only to be recorded in the axial direction.

Initially a rigid sting provided the means of attachment between the rear of the ornithopter and the load sensor; however, vibration induced in the sting by the flapping motion of the model corrupted the recorded results. The sting was therefore replaced with steel wire, which dampened rogue vibrations; and a hanging mass was employed to transmit a positive load via a single pulley. This acted to bias the load such that positive and negative thrust produced by the wings (and drag induced by the flow of air over the model) could be measured. The mass was hung

Ornithopter	A	B
Half-span, $\frac{b}{2}$ (m)	0.325	0.600
Mean chord, $\bar{c}$ (m)	0.151	0.274
Reference wing area, S (m^2)	0.098	0.33
Peak-to-peak flapping amplitude, 2Γ (°)	52	52
Total mass (kg)	0.320	0.460

Table 1: Ornithopter properties

below the floor of the wind tunnel to minimise its drag.

The flapping frequency of the ornithopter was measured using a slotted optical switch positioned near the wing root. On each upstroke, the wing spar interrupted an infrared beam, generating a pulse in the output signal from the switch. The average flapping frequency based on the number of pulses every 1.5 s was then extracted from the signal by a data-acquisition system.

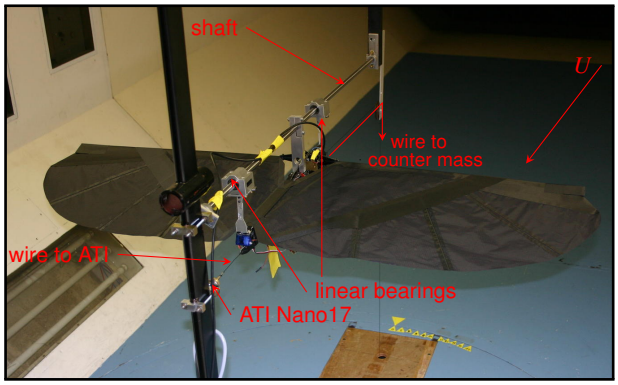

Figure 3: Experimental arrangement, showing Ornithopter A in the wind tunnel.

Procedure

Flow visualisation with smoke was used to examine the flow around upstream components of the test rig. Smoke was generated using an Aerotech SGS-90 system and injected into the tunnel upstream of the test rig. The wakes generated by the upstream bodies were found not to be large enough to affect the air flow in the vicinity of the wings.

Following preliminary characterisation of the flow, the time-dependent thrust produced by each ornithopter was measured for 10 s at a range of flapping frequencies and freestream velocities. The thrust produced by Ornithopter A was measured up to its maximum flapping frequency of 9 Hz; however, measurements were taken with Ornithopter B with a maximum flapping rate of only 6 Hz. Above this frequency, the generated thrust exceeded the range of the load sensor. Both ornithopters were tested in wind speeds up to their maximum flight speed of ~ 9 m/s, based on the manufacturer's specifications [7].

Results

Modelling

The model described above was adapted into a computer code to predict thrust for comparison with the experimental data. In adapting the model, certain aerodynamic characteristics were defined, such as the characteristics of the airfoil, leading edge suction efficiency, drag coefficients and pitch angle. For the purposes of this analysis, the wings were modelled as a flat plate ($\alpha_0 = 0$, $\theta_w = 0$) with a leading-edge-suction efficiency of 0.18 and a maximum stall angle of 13° [6]. While other parameters, such as the amplitude of the flapping motion, were directly measured as indicated in table 1. Furthermore, it was assumed that static negative-α stalling would not occur.

During the experiments the flexibility of the wing was not measured and β_0 was not quantified experimentally. Therefore for the purpose of comparing experimental and predicted thrust values, β_0 was treated as a fit parameter and was estimated using a least-squared-error analysis of the mean thrust measurements. For the measurements taken at flow speed of 9 m/s,

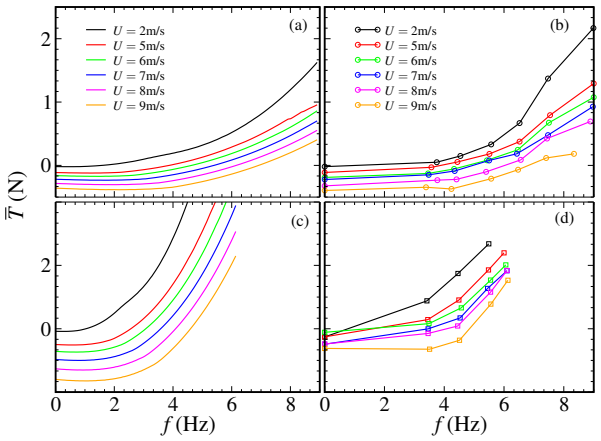

Figure 4: Theoretical and experimental mean net thrust profiles. (a) predicted and (b) measured for Ornithopter A, (c) predicted and (d) measured for Ornithopter B

$\beta_0 = 112°$/m and $\beta_0 = 72.2°$/m returned the best fit across the full frequency range for Ornithopters A and B, respectively. The optimum β_0 was found to increase as the freestream velocity was reduced. However, for the purposes of this analysis, the above values were taken as representative and held fixed across the freestream velocity range.

Mean Thrust

Figures 4a and c show the predicted mean net thrust values for Ornithopter A evaluated with an aerodynamic twist of 112°/m and for Ornithopter B with 72.2°/m, respectively. The experimental and analytical results showed a monotonic increase in the mean net thrust with increasing flapping frequency, as would be anticipated from the basic behaviour of flapping motion. The results also indicated a decreasing net thrust with increasing freestream velocity, due to the increase in drag as the freestream velocity increases. Better agreement between predicted and experimental mean net thrust values was reached at higher freestream velocities. This agreement also tended to be better for Ornithopter A than for B. These observations may be explained by the fact that at low freestream velocities and high flapping rates, the wing-tip speed becomes comparable to or greater than the freestream speed. Under these conditions, unsteady effects play an increasing role aerodynamically.

The deterioration in agreement between the theoretical and experimental results for Ornithopter B may also be caused by the fact that it has approximately twice the wing span of Ornithopter A. Thus at a given flapping frequency, the magnitude of its wing-tip speed is twice as large as Ornithopter A.

As shown in figure 5, for given wing geometry and aerofoil parameters the predicted mean thrust curves were found to collapse onto a curve of the form

$$C_{\overline{T}} = C_{\overline{T}}\left(k, \beta_0 \frac{b}{2}\right) \tag{15}$$

where $k = f\bar{c}/(2U)$ is a reduced frequency, $\frac{b}{2}$ is the wing half-span and $C_{\overline{T}} = \overline{T}/(\frac{1}{2}\rho U^2 S)$ is the mean thrust coefficient, where S is the total wing area. For each ornithopter, the non-dimensionalised experimental data shows reasonably good collapse across the range of k tested. However, within the experimental data, this collapse of the thrust curves only holds for freestream velocities above 2 m/s, because at lower freestream velocities, unsteady effects begin to dominate. While the two ornithopters are geometrically similar, it does not follow that

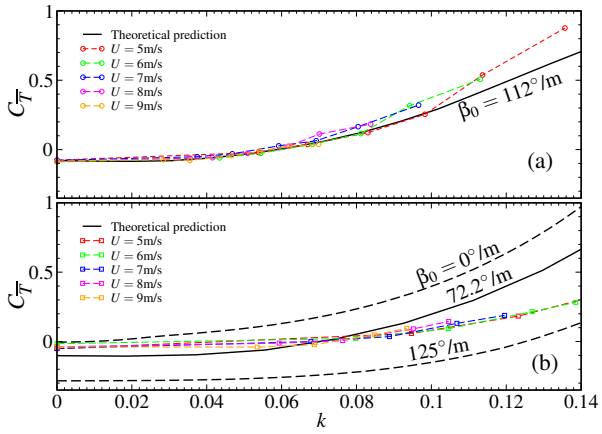

Figure 5: Mean net-thrust coefficient *vs.* reduced frequency for (a) Ornithopter A and (b) Ornithopter B

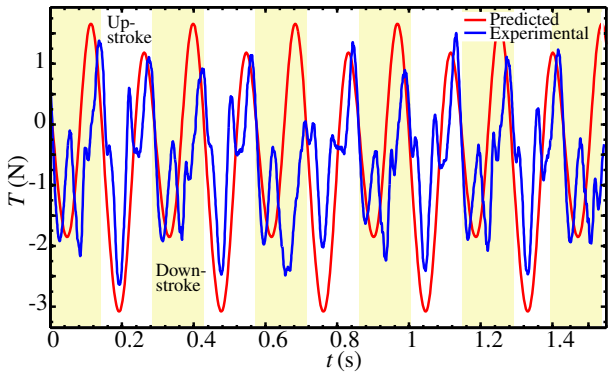

Figure 6: Time-resolved thrust predicted by the model and measured experimentally for $f = 3.51$ Hz and $U = 9$ m/s.

they are structurally similar. Indeed the result of figure 5 indicate a lack of collapse when Ornithopter A and B are compared. This suggests that they have different $\beta_0 b$ values.

Furthermore, figure 5 shows that for optimum β_0, the agreement between the experimental and theoretical profiles is better for Ornithopter A than for B. It could be that, due to the greater inertial forces of Ornithopter B, the magnitude of the twist distribution is more sensitive to changes in k and β_0 does not remain fixed across the frequency range. At lower flapping frequency, the magnitude of the twist distribution remains small; and with increasing frequency, the magnitude of the twist distribution may also increase. This is reinforced by the agreement between the experimental thrust profile at low flapping frequency with the theoretical profile at $\beta_0 = 0$ and agreement at high flapping frequency with a higher β_0 profile.

Thrust Time Histories

Figure 6 shows the measured and predicted time-resolved thrust for Ornithopter B at $U = 9$ m/s and $f = 3.51$ Hz. The time series is for the optimum β_0 (65.6°/m) as established for $U = 9$ m/s and $f = 3.51$ Hz, where unsteady effects are minimised. For the experimental data, the beginning of the stroke cycle was not known, thus its phase has been adjusted to best match the model predictions. Furthermore, results showed a better agreement between experiment and theory when all blade-elements throughout a flap cycle remained within the attached flow regime.

From inspection of figure 6 it is evident that both the measured and predicted time-resolved thrust histories have a dominant frequency content at twice the flapping frequency. The predicted thrust also resolves the lower fundamental flapping frequency of the experimental waveform. However, the model does not resolve the higher frequencies evident in the experimental waveform of figure 6, likely due to the quasi-steady nature of the model. These observations were confirmed by spectral analysis of the predicted and experimental time-resolved thrust.

Conclusions

In this paper, the aerodynamic behaviour of two off-the shelf ornithopters was characterised through analysis and experiment. The results of the analysis indicated that for two dynamically similar systems, the non-dimensional thrust profiles collapse and therefore scaling of the results applies. It was also evident that the aerodynamic model utilised agrees well with experimental data especially in regions of low flapping rate and high freestream velocities, where a quasi-steady analysis is applicable. To further improve the predictive ability of the blade-element model, it is necessary to quantify β_0 experimentally and to explore its dependence on flapping rate and freestream velocity. The model can then be extended to consider the high relative angle of attack and dynamic-stall effects with not only plunging motion but also pitching and account for elastic deformation of the wing.

Acknowledgements

The authors gratefully acknowledge the technical assistance provided by O. Holland, P. Jacquemin and A. Gonzalez.

References

[1] ATI Industrial Automation, 2010, http://www.ati-ia.com (Viewed August 5, 2010).

[2] DeLaurier, J. D., An aerodynamic model for flapping-wing flight, *Aeronaut. J.*, **97**, 1993, 125–130.

[3] Garrick, I. E., Propulsion of a flapping and oscillating airfoil, Technical Report 567, NACA, 1936.

[4] Hoerner, S. F., *Pressure Drag, Fluid-Dynamic Drag*, 1965.

[5] Hu, Z., McCauley, R., Schaeffer, S. and Deng, X., Aerodynamics of dragonfly flight and robotic design, in *Proceedings of the IEEE International Conference on Robotics and Automation*, 2009, 3666–3671.

[6] Kim, D. K., Lee, J. S., Lee, J. Y. and Han, J. H., An aeroelastic analysis of a flexible flapping wing using modified strip theory, in *Proceedings of SPIE, Active and Passive Smart Structures and Integrated Systems*, 2008, volume 6928.

[7] Kinkade, S., Hobbytechnik is flapping flight!, 2010, http://www.flappingflight.com (Viewed August 5, 2010).

[8] Montamed, M. and Yan, J., A reinforcement learning approach to lift generation in flapping MAVs: Experimental results, in *IEEE International Conference on Robotics and Automation*, 2007, 748–754.

[9] Mueller, D., Bruck, H. and Gupta, S., Measurement of thrust and lift forces associated with drag of compliant flapping wing for micro air vehicles using a new test stand design, *Experimental Mechanics*, 1–11.